Resolving the adsorption of molecular O_2 on the rutile TiO_2(110) surface by noncontact atomic force microscopy

Igor Sokolović[a], Michele Reticcioli[a,b,c], Martin Čalkovský[a,d], Margareta Wagner[a,e], Michael Schmid[a], Cesare Franchini[b,c,f], Ulrike Diebold[a], and Martin Setvín[a,g,1]

[a]Institute of Applied Physics, Technische Universität Wien, 1040 Vienna, Austria; [b]Faculty of Physics, University of Vienna, 1090 Vienna, Austria; [c]Center for Computational Materials Science, University of Vienna, 1090 Vienna, Austria; [d]Institute of Physical Engineering, Brno University of Technology, 616 69 Brno, Czech Republic; [e]Central European Institute of Technology, Brno University of Technology, 612 00 Brno, Czech Republic; [f]Dipartimento di Fisica e Astronomia, Università di Bologna, 40127 Bologna, Italy; and [g]Department of Surface and Plasma Science, Faculty of Mathematics and Physics, Charles University, 180 00 Prague 8, Czech Republic

Edited by Cynthia M. Friend, Harvard University, Cambridge, MA, and approved May 7, 2020 (received for review December 20, 2019)

Interaction of molecular oxygen with semiconducting oxide surfaces plays a key role in many technologies. The topic is difficult to approach both by experiment and in theory, mainly due to multiple stable charge states, adsorption configurations, and reaction channels of adsorbed oxygen species. Here we use a combination of noncontact atomic force microscopy (AFM) and density functional theory (DFT) to resolve O_2 adsorption on the rutile TiO_2(110) surface, which presents a longstanding challenge in the surface chemistry of metal oxides. We show that chemically inert AFM tips terminated by an oxygen adatom provide excellent resolution of both the adsorbed species and the oxygen sublattice of the substrate. Adsorbed O_2 molecules can accept either one or two electron polarons from the surface, forming superoxo or peroxo species. The peroxo state is energetically preferred under any conditions relevant for applications. The possibility of nonintrusive imaging allows us to explain behavior related to electron/hole injection from the tip, interaction with UV light, and the effect of thermal annealing.

O_2 | oxides | TiO_2 | nc-AFM | tip functionalization

Interaction of O_2 with metal oxide surfaces plays a key role in many applications including gas sensing (1), heterogeneous catalysis (2), the oxygen evolution (3) and oxygen reduction reactions (4), and memristive switching (5). Rutile TiO_2(110) is considered a prototypical metal oxide surface (6), and adsorption of molecular oxygen on this material has attracted a lot of attention over the past decades (7–14). Despite extensive work on this fundamental problem even basic O_2 adsorption configurations have remained unclear, which has led to puzzling observations regarding the thermal chemistry and photochemistry of this important molecule. We demonstrate that the superior resolution and nonintrusive imaging possible with noncontact atomic force microscopy (nc-AFM) (15) allow resolving these open questions.

Within the last decade, nc-AFM has achieved tremendous success, including submolecular imaging of organic molecules (16), chemical discrimination of surface atoms (17), and measuring and manipulating the charge state of single atoms and molecules (18). While nc-AFM is an ideal tool for studying metal oxides, it is not yet as widely employed as one could expect. The main impediment is the strong tip dependence of the AFM images; there is no well-established tip functionalization suitable for metal oxide surfaces, unlike, for example, the CO-terminated tips regularly used for imaging organic molecules (19, 20). Our work reveals a purposed tip functionalization by an O adatom as a very promising approach. Such tips allow imaging the surface oxygen sublattice in the repulsive regime without chemical interaction with either the substrate or the oxygen adsorbates and provide excellent lateral resolution.

Oxygen molecules prefer dissociative adsorption when dosed on a TiO_2(110) surface with oxygen vacancies (V_O) at room temperature (21–28). On the other hand, the results of low-temperature O_2 dosing (<150 K) are ambiguous: Scanning probe techniques mostly report dissociative adsorption (28–31), while area-averaging techniques show a strong preference for molecular adsorption (31–44). The adsorption of molecular O_2 inside a V_O was the first adsorption hypothesis confirmed experimentally (45–49) and calculated to be the preferred configuration (50–56). Later, it was deduced that O_2 molecules can also chemisorb to the rows of fivefold-coordinated Ti atoms (Ti_{5c}) (47–49), while density functional theory (DFT) calculations mostly predict these species as the second most favorable molecular adsorption configuration (50–59). The exact O_2 adsorption configurations, however, and the temperature range in which they are present still remain unclear. The standard analysis technique, scanning tunneling microscopy (STM), can easily dissociate the adsorbed molecules and requires very gentle conditions to avoid manipulation of the molecular O_2 (45–49). Using a nonintrusive local nc-AFM technique has already proved promising by observing one O_2 molecular species on the Ti_{5c} rows (26, 27). The functionalization of the nc-AFM tip by an

Significance

Molecular O_2 on semiconducting metal oxides, its adsorption, response to thermal treatment, UV irradiation, and electron/hole injection is at the heart of a wide range of technologies. These processes were studied molecule by molecule on the prototypical model oxide TiO_2(110), using noncontact AFM. We show that the nonintrusive nature of the nc-AFM and its exceptional spatial resolution due to the functionalization of the tip with a terminal O atom allow identifying oxygen adsorption geometries which were not previously determined by other techniques. In combination with density functional theory calculations, we explain the charge states of the various adsorbed oxygen species, their dynamics upon annealing and UV irradiation, and the role of electron exchange with the TiO_2 substrate.

Author contributions: I.S., M.R., M. Schmid, C.F., U.D., and M. Setvín designed research; I.S. and M.R. performed calculations and simulations; I.S., M.Č., M.W., and M. Setvín conducted measurements; and I.S., M.R., M.Č., M.W., M. Schmid, C.F., U.D., and M. Setvín wrote the paper.

The authors declare no competing interest.

This article is a PNAS Direct Submission.

[1]To whom correspondence may be addressed. Email: setvin@iap.tuwien.ac.at.

This article contains supporting information online at https://www.pnas.org/lookup/suppl/doi:10.1073/pnas.1922452117/-/DCSupplemental.

First published June 11, 2020.

O atom provides higher resolution. Our study reveals that there are, in fact, three distinct O_2 species on the surface, one in the vacancy and two at the Ti_{5c} rows, coordinated to either one or two Ti atoms. Each of these species shows a different behavior upon annealing or UV light irradiation.

On stoichiometric TiO_2(110) surfaces, the molecular O_2 only physisorbs (60, 61). Electron donation from the surface, resulting in an O_2 anion, is required for the chemisorption (59). The surface excess electrons mostly originate from the intrinsic bridging oxygen vacancy defect (V_O), but can also be provided either by coadsorbates (for example, OH) or by titanium interstitials (Ti_{int}) (59). The charge state of the adsorbed O_2 molecules has been discussed for a long time with major disagreement between experiment and theory. While theory mostly finds the adsorbed molecules to be doubly negative, i.e., in the peroxo state (50–53, 57–59), experimental data were often interpreted as singly charged negative, i.e., superoxo molecules (37–43, 48). The charge state of the adsorbed O_2 affects the adsorption geometry. Our highly resolved data allow a direct comparison with calculation results, confirming the predicted peroxo state.

Chemisorbed molecular O_2 was observed to desorb from the surface at ≈400 K in temperature-programmed desorption (TPD) experiments (31–33, 37, 39), yet the origin of this peak remains clouded due to the diffusion of titanium interstitials from the bulk that is also activated close to this temperature (28, 33, 62). In annealing excursions, we follow the different O_2 species in detail and identify their fate.

In contrast to the sharp peak in TPD, the desorption of molecular O_2 under UV light shows fast initial O_2 desorption followed by a long tail of slowly desorbing O_2 molecules (37–43). Via direct observation of the photoinduced O_2 reaction products after short and long UV light (UV) exposures, we determine which molecules contribute to the fast and slow desorption channels. In combination with tip-induced charge injection experiments, we also clarify the hole- or electron-induced nature of the various processes and whether a one- or two-step process is at work.

The three coexisting molecular species, and their adsorption properties and dynamic behavior, explain the rich surface chemistry of O_2 on TiO_2(110). Our tip functionalization, verified in quantitative force–distance curves above various adsorbates, should prove invaluable for future AFM investigations on oxide surfaces.

Results

O_2 Adsorption Configurations. The constant-height AFM images in Fig. 1 *A* and *B* show the rutile (110) surface with adsorbed oxygen. The image contrast is predominantly formed by repulsion between the O-functionalized tip apex and surface O atoms. The geometrically protruding rows of surface bridging oxygen (O_{br}) atoms are clearly resolved, occasionally interrupted by oxygen vacancies (V_O) (6). Such an image contrast provides direct access to the oxygen anion sublattice of the surface and complements the cation sublattice contrast typically obtained in STM imaging (63).

Fig. 1*A* shows a surface with an initial concentration of oxygen vacancies of $c_{Vo} \approx 0.05$ monolayers (ML), subsequently exposed to 0.1 Langmuir (L) of O_2 at a sample temperature of 10 K (measured at 4.8 K). Some oxygen vacancies remain unoccupied (marked with a white circle in Fig. 1*A*), while others are populated with an O_2 molecule (marked by a purple circle in the AFM images in Fig. 1 *A* and *B*). These molecules are adsorbed with their bond axis in the $[1\bar{1}0]$ direction, perpendicular to the direction of the O_{br} rows. The appearance of these molecules in the AFM images indicates that they lie flat, incorporated in an O_{br} row. There are two molecularly bound O_2 species on the Ti_{5c} rows (O_2/Ti_{5c}), both flat according to the equal frequency shift over the constituent atoms inside each molecule. The molecule with its bond axis aligned parallel to the [001] direction of O_{br} rows (marked with a green circle in the AFM images in Fig. 1*A*) is bound to two underlying, neighboring, Ti_{5c} atoms. The molecule with the bond axis rotated by 45° toward the O_{br} rows (marked with an orange circle in the AFM images in Fig. 1*A*) is bound to only one Ti_{5c} atom directly underneath. We use the following nomenclature for the molecules: ω for the molecules inside the oxygen vacancy, π for the molecules parallel to the O_{br} rows, and τ for the molecules turned toward the O_{br} rows. We note that τ and π molecules are not only differently rotated but also in different adsorption sites, shifted half a unit cell along [001].

The last species present in Fig. 1*A* are oxygen adatoms (marked with a red square in the AFM images), originating from dissociation of molecular oxygen. Oxygen does not spontaneously dissociate at this temperature. In Fig. 1*A*, oxygen adatoms were created by tip-induced dissociation to have all species present in a single image. Here, a voltage pulse of +1.3 V was applied to dissociate one π molecule. The adatoms commonly appear as isolated spheres located directly above one Ti_{5c} atom (red square in Fig. 1*B*). Their unusual, asymmetric contrast in Fig. 1*A* is a consequence of their mutual proximity and tip bending (64, 65).

Fig. 1 *C–G* shows DFT+U (U is the Hubbard onsite Coulomb interaction) results for the optimized geometries and corresponding density of states (DOS) of the various molecular configurations and the oxygen adatom present on the surface. Calculated adsorption energies E_{ads}, oxygen bond lengths $d(O_2)$, Bader charges Q_B, and spin states of the adsorbates are summarized in the table in Fig. 1*H*. The calculations were performed by adsorbing a single O_2 or O on a reduced 6×2 surface slab with one V_O. This corresponds to a V_O concentration of 1/12 ML (= 8.3%), similar to the experimental conditions. Fig. 1*C* shows the ground state of the reduced slab as a starting point of each adsorption scenario. The oxygen vacancy is a donor, which provides two excess electrons to the slab. These electrons form small polarons due to their coupling with lattice distortions, and they preferentially localize on the next-nearest subsurface Ti_{6c} atoms (66–69). They form the characteristic Ti^{3+} in-gap states in the calculated DOS shown in Fig. 1*C*, *Left* and enlarged in Fig. 1*C*, *Inset*, while their spatial distribution (Fig. 1*C*, *Right*) confirms their localization on polaron-hosting subsurface sixfold-coordinated titanium atoms (Ti_{6c}). The presence of adsorbates can significantly affect the polaronic ground state of this surface (70). Fig. 1 *D–G* shows the slab after adsorbing the oxygen species in geometries corresponding to the AFM measurements (τ, π, ω, and O_{ad}, respectively), with the DOS plots and structure images organized as in Fig. 1*C*. Common to the presence of all adsorbed species is depletion of the polaron state. As a consequence, there is a dramatic change of the in-gap state of the clean, reduced slab; the in-gap state even shifts into the valence band in Fig. 1 *F* and *G*.

The τ molecule (Fig. 1*D*) is calculated to have the weakest adsorption energy, followed by the π molecule (Fig. 1*E*). Both molecules preserve an in-gap state in the total DOS. The origin of the in-gap state, enlarged in Fig. 1 *D* and *E*, *Insets*, clearly illustrates a charge transfer from the polaron-hosting Ti_{6c} sites to the $2\pi^*$ orbitals of the adsorbed molecules. The spatial distribution of these two in-gap electrons is illustrated in Fig. 1 *D* and *E*, *Right*. They are shared between the constituent atoms of the O_2 molecule and preserve their opposite spins, yielding a zero net magnetization on the molecule. Therefore, both π and τ molecules accept two available polaronic electrons from the slab, making them peroxo molecules O_2^{2-}. Bader charges (71) of the covalently bound adsorbates are usually significantly lower than the oxidation states (72–74), since they do not account for the electrons used in the covalent bond formation to the underlying Ti atom(s). A Bader charge of the molecules (sum of Bader charges of the constituent atoms) of $Q_B \approx 1$ implies that roughly

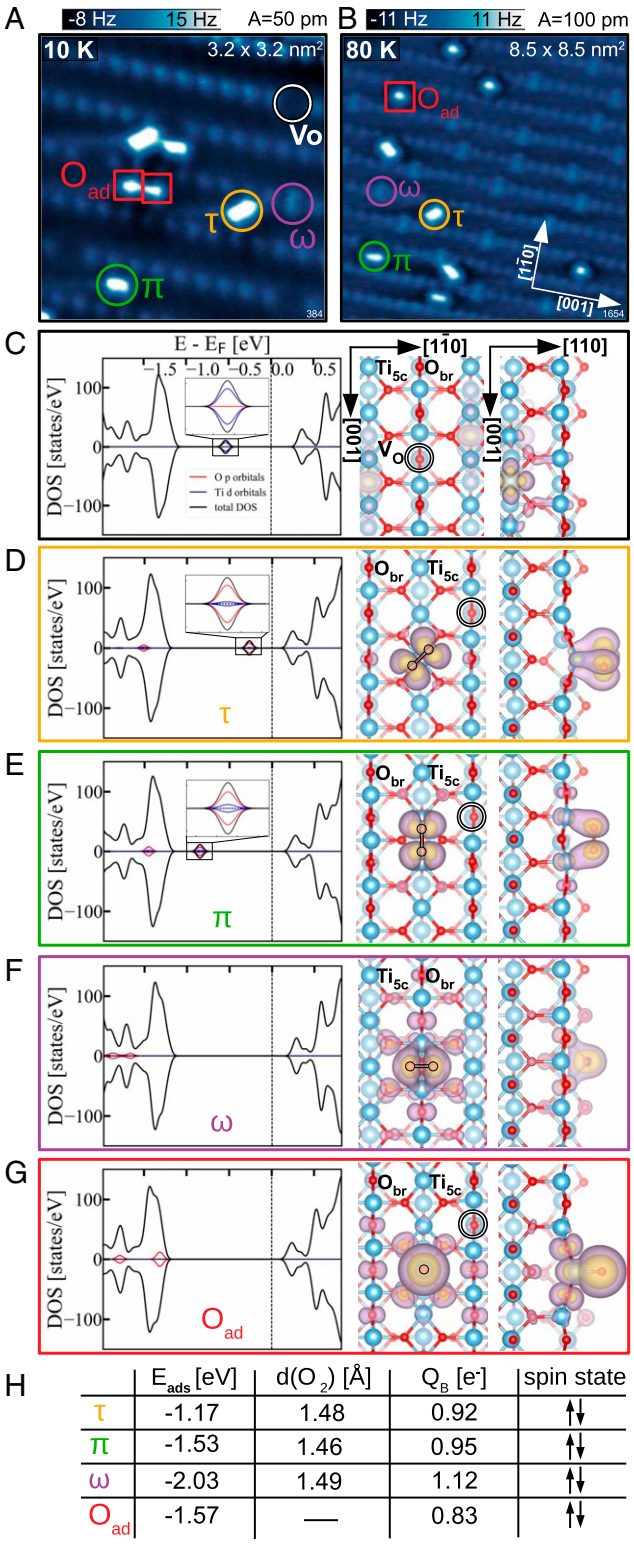

	E_{ads} [eV]	d(O_2) [Å]	Q_B [e⁻]	spin state
τ	-1.17	1.48	0.92	↑↓
π	-1.53	1.46	0.95	↑↓
ω	-2.03	1.49	1.12	↑↓
O_{ad}	-1.57	—	0.83	↑↓

Fig. 1. Adsorbed molecular O_2 and atomic O. (*A* and *B*) Constant-height AFM images obtained after O_2 dosing at 10 K and 80 K, respectively, showing adsorbed molecular O_2 (circles) and atomic O species (squares). (*C*) DFT calculation of the polaronic ground state of the clean, reduced surface with one bridging-oxygen vacancy. (*Left*) The total DOS (black) and the partial contributions of the adsorbed O atoms (red) and their nearest Ti atoms (blue). The in-gap state is magnified in *Inset*. (*Right*) Partial charge-density plots showing the top and the side view of the charge distribution of the two excess electrons originating from the V_O. (*D*–*G*) DFT calculations of the molecular O_2 (*D*–*F*) and atomic O (*G*) adsorption configurations marked in constant-height AFM images, together with their respective names in the nomenclature adopted throughout this paper. (*H*) Table summarizing the adsorption energy E_{ads} and spin states of the adsorbates; O–O bond lengths $d(O_2)$ and Bader charges Q_B of the τ, π, and ω molecules; and the Bader charge Q_B of the oxygen adatom O_{ad}.

one electronic charge is spent on creating two chemical bonds to the underlying Ti atom(s) to which these molecules are directly bound. The calculated bond lengths of 1.46 and 1.48 Å for the π and τ molecules, respectively, are larger than gas-phase O_2 (DFT value 1.28 Å) and support their peroxo assignment (75).

The calculated molecular species with the highest adsorption energy is the ω molecule (Fig. 1*F*). This adsorption configuration is characterized by the disappearance of the in-gap state and the corresponding states are shifted deep into the valence band. The spatial charge-distribution plot in Fig. 1*F* shows the sum of all p-type contributions from the molecular states of the ω molecule. Due to the complete disappearance of the in-gap state and the appearance of symmetric features in the projected DOS on this molecule, we conclude that two excess electrons of opposite spin, present in the reduced slab, have been transferred to the ω molecule, again making it a peroxo O_2^{2-} species. A calculated bond length of 1.48 Å, no net magnetization, and a Bader charge larger than 1 confirm the charge transfer and peroxo character.

Simulating adsorption of an isolated oxygen adatom on top of a Ti_{5c} atom (Fig. 1*G*) also shows the disappearance of the in-gap state. The p-type states associated with the adatom are shifted to the valence band and indicate the transfer of all of the excess electrons to the adatom, making it a doubly negative ionosorbed O_{ad}^{2-} atom. All adsorbed species in Fig. 1 *D*–*G* were placed in their minimum-energy positions with respect to the empty V_O (*SI Appendix*, Fig. S1).

Fig. 1*B* shows the surface after dosing 0.5 L of oxygen at $T = 80$ K. At these conditions, all oxygen vacancies are filled by ω molecules, and additional π and τ molecules adsorb on the Ti_{5c} rows. The saturation coverage of these π and τ molecules amounted to another 0.5× to 1× the V_O concentration throughout our experiments. This could mean either that some of the molecules are in a superoxo charge state or that additional electrons are provided by the bulk dopants. In our calculations, adding another O_2 molecule to the slabs shown in Fig. 1 does not result in chemisorption; the excess electrons provided by the oxygen vacancy are already consumed by the first peroxo species. Doping the slab by including extra electrons, in addition to the existing ones, allows further chemisorption of molecules (*SI Appendix*, Fig. S2).

In Fig. 2 we investigated the adsorption configurations of superoxo species. The superoxo species were formed by coadsorbing two molecules in configurations corresponding to a peroxo charge state to the slab containing one V_O. The spin-projected DOS of the coadsorbed pairs of molecules is now characterized by two empty spin-down in-gap states, one for each adsorbed molecule, while the populated spin-up states associated with the molecules are located within the valence band. Projected partial-charge-density plots associated with the spin-down, in-gap empty states are plotted in Fig. 2 *A* and *B*, *Right*. These empty states have the symmetry of the antibonding $2\pi^*$ orbital and illustrate the spatial distribution of the filled spin-up $2\pi^*$ states at each molecule. The table in Fig. 2*C* quantifies the properties of the adsorbed superoxo species. The adsorption energy per molecule implies chemical bonding of the superoxo species, but in a metastable state at this level of theory, due to the weaker adsorption energies than those of single peroxo species adsorbed to the same slab. The bond lengths of the coadsorbed molecules agree with the expected values for superoxo species (75), as do the Bader charges equal to one-half of the Bader charges for the

PHYSICS

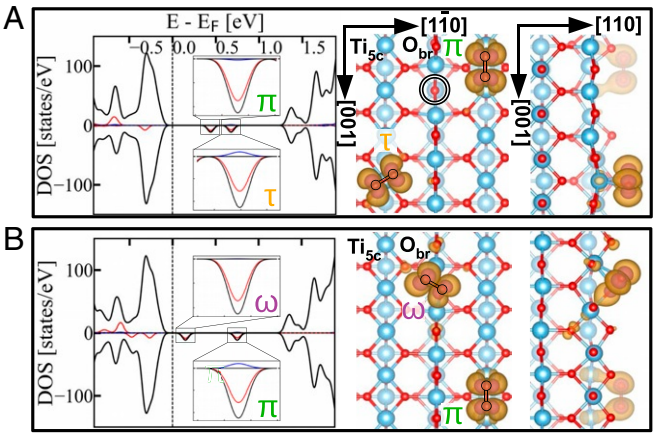

C

	E_{ads} [eV]	d(O_2) [Å]	Q_B [e^-]	spin state
π & τ	-0.69 per O_2	1.38	0.58	↑
		1.39	0.48	↑
ω & π	-0.74 per O_2	1.39	0.66	↑
		1.38	0.57	↑

Fig. 2. Stable superoxo species. (*A* and *B*) Calculations of the coadsorption of π and τ molecules (*A*) and ω and π molecules (*B*) to the slab with one V_O. In *A* and *B*, *Insets* in the calculated DOS magnify the unoccupied in-gap states residing on the adsorbed molecules, and the partial-charge-density plots show the spatial distribution of these unoccupied in-gap states. (*C*) Table summarizing the adsorption energy per molecule E_{ads}, the bond length $d(O_2)$, Bader charge Q_B, and the spin state of each molecule in the coadsorption calculations.

peroxo species. Singly charged oxygen adatoms O_{ad}^- could not be stabilized employing the methods used to calculate the other peroxo and superoxo species (Figs. 1 and 2), and we conclude that they are unstable or at least not preferable.

Comparison of the calculated and experimentally observed geometries of superoxo and peroxo ω and τ molecules indicates their charge state on the surface: Calculated superoxo ω and τ molecules have a rotational angle of 60° with respect to the O_{br} rows, which does not correspond to the angles measured in the AFM images. On the other hand, the geometry of the calculated peroxo ω and τ molecules does correspond to the experimental observations: Peroxo ω molecules are perpendicular to the O_{br} row, and the peroxo τ molecules are rotated toward the O_{br} row by 45° (more detailed comparison in *SI Appendix*, Fig. S3). Therefore, we assign the ω and τ molecules to the energetically more favorable peroxo ω^{2-} and τ^{2-} states. The calculated geometry of the superoxo and peroxo π molecules differs only in the bond length, by values too small for the resolution of the AFM images (limited by the convolution of the tip apex shape and the shape of the adsorbate). Experimentally, we do not observe a preference for either the π or the τ molecules, which indicates their similar adsorption energies. Therefore, we must assume that the π molecules are adsorbed in the energetically favored peroxo π^{2-} state as well. The geometry of the oxygen adatoms cannot be used to determine their charge state in a similar manner to that for the ω and τ molecules. According to calculations, doubly ionized singlet O_{ad}^{2-} is the only stable species (*SI Appendix*, Fig. S2), and hence we assign the charge of oxygen adatoms accordingly. The absence of theoretically metastable superoxo species on the surface exposed to 0.5 L of O_2 at the temperature of 80 K (Fig. 1*B*) implies that, once the peroxo species is adsorbed, it will not share charge with the next molecule that arrives to the surface. Furthermore, the calculated adsorption energies of the peroxo and superoxo species (Figs. 1*H* and 2*C*) show that if the coadsorption of two superoxo species were to occur in our experiments, it is energetically favorable for one superoxo molecule to donate an electron to the other one and subsequently desorb, resulting in a surface with exclusively peroxo O_2^{2-} species.

Annealing. Annealing of the surface reveals the gradual activation of various O_2 dissociation channels. Fig. 3 *A*–*C* shows constant-height AFM images taken after exposing the sample to O_2 at 80 K, followed by annealing to different temperatures and subsequent cooling to the measurement temperature of 80 K. The amount of adsorbed O_2 is close to the saturation coverage. The statistics in Fig. 3*D* were collected by counting the number of each species $N(x)|x \in \{\omega, \pi+\tau, O_{ad}\}$ in at least two representative 60-nm^2 images at each given temperature and normalizing this number to the number of oxygen vacancies $N(V_O)$ on the respective images (error bars in the stacked bar graphs are equal to $\sqrt{N(V_O)}$). The histogram at each temperature is divided into two columns. The left column represents the total number of oxygen vacancies obtained as a sum of empty oxygen vacancies, ω molecules, and isolated O_{ad} atoms, which are the product of the well-known "vacancy-healing" dissociation channel (21, 29, 30, 45). The right column is the sum of the total number of π and τ molecules and the number of O_{ad} pairs on the same Ti_{5c} row ($2\times O_{ad}$), which are the products of a dissociation channel

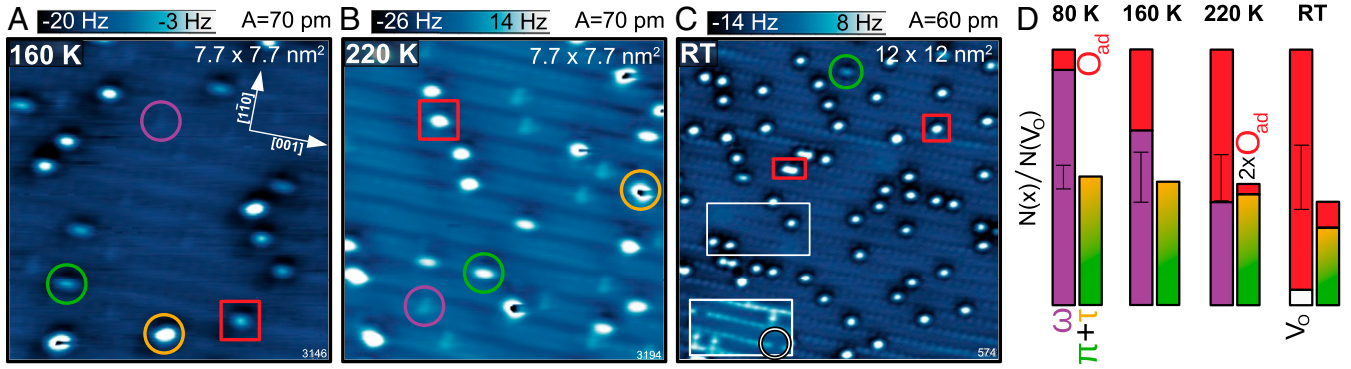

Fig. 3. Stepwise annealing of TiO_2(110) with a close-to-saturation coverage of O_2 dosed at 80 K. (*A*–*C*) AFM images (taken at 80 K) after annealing to a temperature of (*A*) 160 K, (*B*) 220 K, and (*C*) room temperature (RT). The adsorbed species are marked with the same colors and symbols as in Fig. 1, with one red rectangle in *C* marking a pair of O adatoms ($2\times O_{ad}$). *Inset* in *C* is an AFM image of the white rectangle imaged closer to the surface, showing an empty V_O more clearly. (*D*) Number of adsorbed species $N(x)|x \in \{\omega, \pi+\tau, O_{ad}\}$ at each annealing temperature. Both columns are normalized to the number of (empty and filled) oxygen vacancies $N(V_O)$ on the surface.

along the Ti_{5c} rows (62), normalized to the concentration of oxygen vacancies as well. The observed, thermally induced reactions, together with the range at which their respective onset temperatures T_{min} fall, can be summarized as

$$\begin{aligned}
\omega &\xrightarrow{+T} O_{ad} + O_{br} \quad ; \quad 10\,K < T_{min} < 80\,K \\
\pi &\xrightarrow{+T} 2 \times O_{ad} \quad ; \quad 160\,K < T_{min} < 220\,K \\
\tau &\xrightarrow{+T} 2 \times O_{ad} \quad ; \quad 160\,K < T_{min} < 220\,K \\
\omega &\xrightarrow{+T} O_2(gas) + V_O \quad ; \quad 220\,K < T_{min} < 300\,K.
\end{aligned} \qquad [1]$$

There is no spontaneous appearance of O_{ad} after dosing O_2 at 10 K (the O_{ad} pair in Fig. 1*A* comes from deliberate O_2/Ti_{5c} dissociation), while the surface exposed to O_2 at 80 K (Fig. 1*B*) does show a small concentration of isolated O_{ad}. Dissociation of the ω molecules, which heals the oxygen vacancy and leaves an isolated O_{ad}, is therefore active at temperatures below 80 K. This dissociation channel is further promoted by thermal annealing, and already at 160 K the concentration of ω molecules has notably decreased, followed by a proportional increase of the O_{ad} coverage. This trend continues through the 220-K temperature and no ω molecules are left after room temperature (RT) annealing. Most of them dissociated with the resulting concentration of isolated O_{ad} close to the initial concentration of oxygen vacancies. Additionally, a small fraction of oxygen vacancies reappear empty, indicating a possible weak desorption channel of ω molecules to the gas phase (O_2(gas)). Empty V_Os were never observed straight after dosing 0.5 L of O_2 at 80 K.

The dissociation of π or τ molecules through the dissociation channel along the Ti_{5c} rows becomes active above 160 K. After annealing the surface to 220 K, O_{ad} pairs appear. With increasing temperature up to RT, their concentration continues to increase at the expense of the π or τ molecules. Both π and τ molecules are still present on the surfaces after RT annealing, indicating a higher activation energy for dissociation compared to the ω molecules.

UV Irradiation. Fig. 4 shows the effect of UV light irradiation on the surface exposed to O_2 at 80 K. The wavelength of the incoming light is sufficient to overcome the 3-eV band gap of TiO_2 and generate electrons and holes responsible for the observed photochemistry. Fig. 4*A* is the starting point of this experiment. The highlighted species in Fig. 4*A* are a guide to the eye for following the reactions after a low dose of UV irradiation (20 W for 20 s), resulting in the surface shown in Fig. 4*B*. The oxygen adatoms are unaffected by UV irradiation irrespective of the dose and provide reference patterns (red squares in Fig. 4) for locating the same region on the surface after the UV irradiation. Following the evolution of the highlighted molecular species from Fig. 4 *A* and *B* reveals that very few ω molecules dissociated and left one adatom right next to the now-healed vacancy. Dissociation of π and τ molecules was not observed. They remained unaffected, switched the configuration between each other, or molecularly desorbed (marked by diamonds in Fig. 4*B*). The observed reactions under the first UV dose of 20 W can be summarized as

$$\begin{aligned}
\omega &\xrightarrow{UV} O_{ad} + O_{br} \\
\pi &\xrightarrow{UV} O_2(gas) \\
\pi &\xrightarrow{UV} \tau \\
\tau &\xrightarrow{UV} O_2(gas) \\
\tau &\xrightarrow{UV} \pi.
\end{aligned} \qquad [2]$$

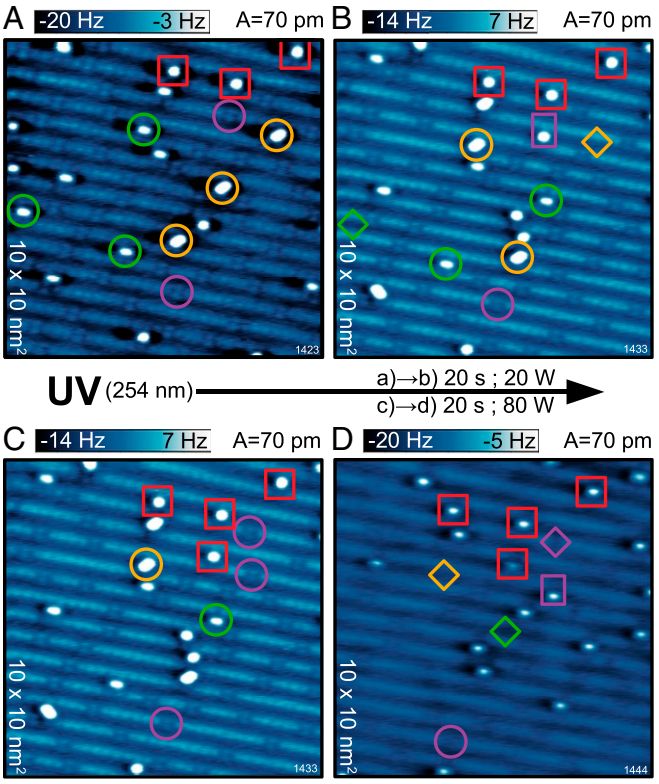

Fig. 4. Effect of UV light irradiation. (*A*) AFM image of the surface after O_2 exposure at 80 K. The adsorbed species are marked with the same colors and symbols as in Fig. 1. (*B*) The same region as in *A* after 20 W UV irradiation for 20 s. The comparison of highlighted species in *A* and *B* reveals the reactions after the low-UV dose. Diamonds mark molecular desorption, and rectangles mark dissociation. (*C*) The same image as in *B* but with different adsorbates highlighted. (*D*) The same region as in *B* and *C* after additional 80 W UV irradiation for 20 s. The comparison of highlighted species in *C* and *D* reveals the reactions after the increased UV dose.

Applying an additional UV dose of 80 W for 20 s has a stronger impact on the adsorbed O_2; see the transition in Fig. 4 *C* and *D*. All π and τ molecules desorbed (with the exception of a single τ molecule per 121 nm^2 of the surface). Therefore, molecular desorption is the end product of O_2/Ti_{5c} photochemistry. On the other hand, the ω molecules started desorbing as well under increased UV dose:

$$\omega \xrightarrow{UV} O_2(gas). \qquad [3]$$

Most of the ω molecules still either remained adsorbed or dissociated, similar to their behavior under a small UV dose. The process of molecular desorption of ω molecules under UV illumination demonstrates a lower cross-section than the desorption of π or τ molecules and constitutes a "slow" desorption channel, which has been reported to be active for even larger UV photon doses (39). Thus, the end product of O_2 photochemistry is a surface with no molecular species adsorbed, but a rather clean surface with a few oxygen vacancies and adatoms.

Tip-Induced Dissociation and Desorption. Fig. 5 shows dissociation events induced by electron injection. The AFM image in Fig. 5*A* shows the O_2-covered surface at 80 K. Applying a +3.0-V sample bias pulse over a point on this surface dissociates most of the molecules in the vicinity, as revealed by the AFM image in Fig. 5*B*. Fig. 5 *A* and *B* illustrates one of the difficulties of studying this adsorption scenario using STM alone. Besides

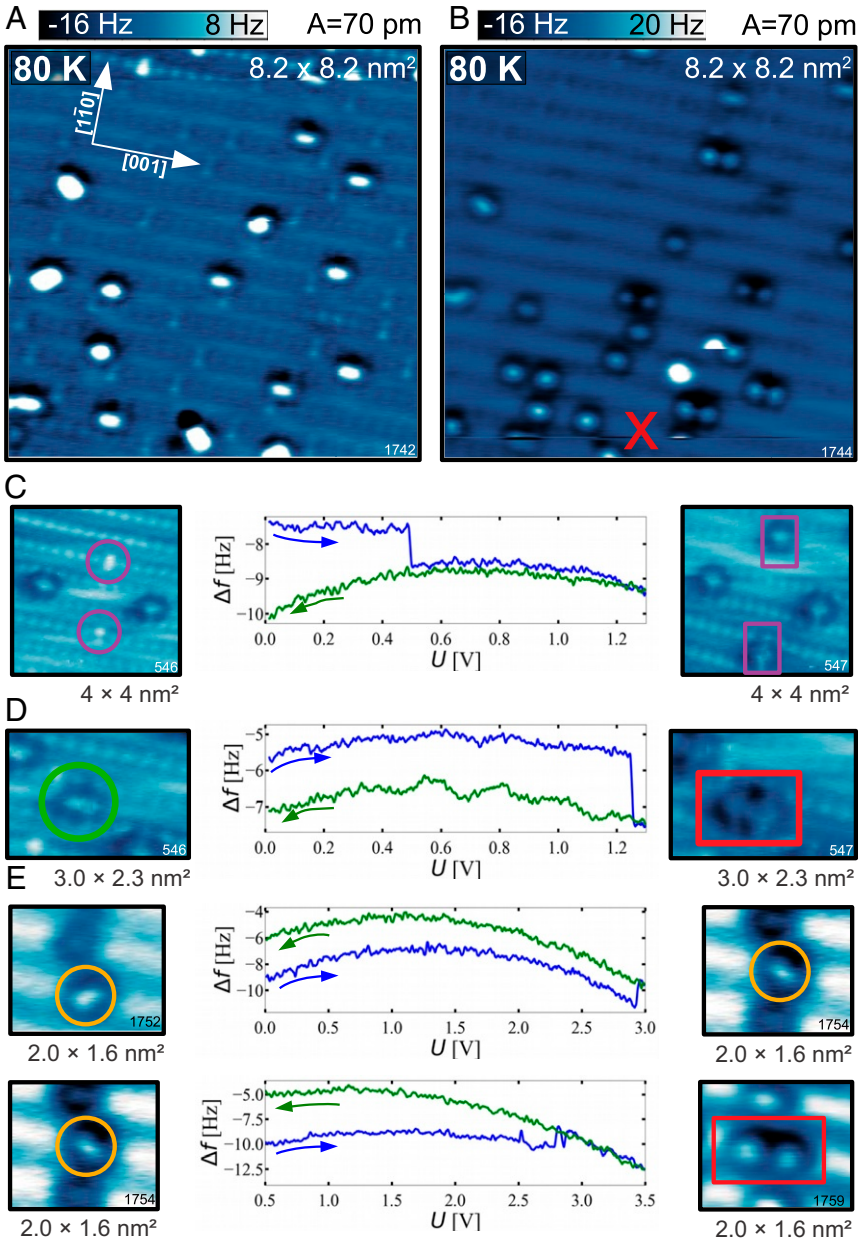

Fig. 5. Tip-induced dissociation. (*A*) AFM image of the O_2-covered surface. (*B*) AFM image of the same area as in *A*, after a +3-V bias pulse at the spot marked by the red "x." (*C–E*) AFM images of the ω, π, and τ molecules, respectively, before (*Left*) and after (*Right*) tip-induced dissociation. The frequency shift vs. bias voltage graphs, showing the forward and backward bias ramp, are shown in *C–E*, *Center*. The τ molecule shown in *E* was observed to either rotate (top) or dissociate (bottom).

dissociating the molecules, submolecular resolution in STM is extremely rare and can be obtained only in immediate proximity to the surface where the tip flexibility contributes to the contrast (76–78)—see the constant current STM image shown in *SI Appendix*, Fig. S4. Molecular species were also deliberately dissociated in a more controlled fashion (Fig. 5 *C–E*) by ramping the sample bias voltage in the positive direction. In this case, the underlying adsorbate can experience a change due to tunneling from the tip to the unoccupied states of the adsorbate. This changes the frequency shift vs. bias curve (Kelvin parabola) (79) above the adsorbate due to the changed electrostatic forces acting on the tip $\left(O_2^{2-} \rightarrow 2 \times O^{2-}\right)$. Taking AFM images before and after the positive sample bias ramps confirms that all molecular adsorbates can dissociate. The bias voltage necessary for dissociation varies for different species: ω molecules typically dissociate at a bias of +0.3 to +0.5 V (Fig. 5*C*), π molecules at a bias of 1.25 V (Fig. 5*D*), and the τ molecules at a bias around +3.0 V (Fig. 5*E*). We observed that τ molecules can either rotate (Fig. 5*E*, *Top*) or dissociate (Fig. 5*E*, *Bottom*) at bias voltages close to +3.0 V, and several consecutive rotations can be seen in *SI Appendix*, Fig. S5.

Fig. 6 shows desorption events of all three species, induced by negative sample bias ramps. In this case, electrons are removed (holes are injected) directly above the adsorbed molecules, leading to their desorption. The hole-induced desorption of oxygen is a well-accepted scenario (42, 48), so we did not perform extensive systematic experiments in this direction. Additionally, the desorbing molecule has a high probability of readsorbing at the tip apex, thus destroying the tip functionalization. Therefore, these desorption experiments were performed with the tip retracted

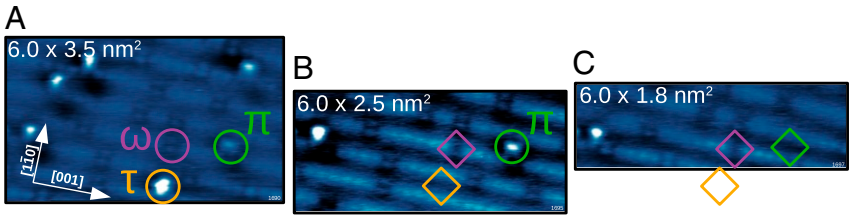

Fig. 6. Tip-induced desorption. (*A*) AFM image of the O_2-covered surface. (*B*) AFM image of the same region after negative bias was ramped above the ω and τ molecules causing their desorption. (*C*) AFM image of the same region after negative bias was ramped above the π molecule causing its desorption.

2 Å from the surface and we present only data where the resulting frequency shift vs. bias curves did not show any changes before and after desorption. The bias was ramped down to a minimum of −3.0 V for desorption of ω and τ molecules (between Fig. 6 *A* and *B*) and down to a minimum of −2.0 V for desorption of the π molecule (between Fig. 6 *B* and *C*).

The STM-induced events are qualitatively similar to the UV-induced events (electron-induced dissociation and hole-induced desorption), but there are differences between the two approaches. The configuration switch between π and τ molecules and vice versa was never achieved using the STM tip.

Force–Distance Curves. All AFM images shown in this paper were measured with the same tip functionalization. This tip consistently displays a characteristic contrast over the adsorbed O_2 molecules and also provides excellent resolution of the oxygen sublattice of the substrate. To better understand this unique tip functionalization, we measured force–distance curves above all of the species and compared them to DFT+U calculations.

Fig. 7*A* shows the experimentally measured force–distance $F(z)$ curves above all surface species. The positions of the minima in the $F(z)$ curves are related to the relative heights of the different adsorbed species: The τ molecule is the highest one, followed by the O_{ad} and the π molecule, while the lowest-lying ω molecule lies in plane with the O_{br} rows (The force minimum above the O_{br} is taken as zero in the z scale in Fig. 7). Fig. 7*B* compares the minima of the experimental $F(z)$ curves (Fig. 7*B*, *Left*) with the vertical heights of the molecules corresponding to the relaxed slabs in Figs. 1 and 2 (Fig. 7*B*, *Right*).

The maxima of the experimentally measured attractive forces above the species are in the order of tens of piconewtons; i.e., the curves were obtained by a chemically inert tip. This is consistent with the oxygen-terminated TiO_2 tip apex obtained by our purposeful tip functionalization. Therefore, we used an oxygen-terminated $(TiO_2)_5$ cluster tip (Fig. 7*C*, *Inset*), developed in previous works (80–82) to explicitly simulate the experimental force–distance curves. These calculated $F(z)$ curves are plotted in Fig. 7*C* and the setup for calculating the $F(z)$ curves is explained in more detail in *SI Appendix*, Fig. S6. Movies S1–S6 show the simulated tip approach.

In Fig. 7*D*, we constructed a simulated constant-height AFM image of the surface using only the simulated $F(z)$ curves in Fig. 7*C* and the geometries of the adsorbed species from Fig. 1 *C*–*G*. Two-dimensional maps of the force above the O_2-covered surface at different heights were constructed by calculating the pairwise interaction between each of the constituent atoms of the surface and the adsorbates with the O-terminated apex of the tip. The force maps within the range of heights spanned by the oscillation amplitude A, $F(z \in [h-A, h+A])$, were converted to a constant-height frequency shift image $\Delta f(h = const.)$ at the distance of 2.6 Å from the O_{br}, by using the small-oscillation-amplitude approximation (83). The simulated frequency shift is larger by a factor of 5 when compared to the highly resolved experimental AFM images, because the DFT+U calculations overestimated the protrusion of each species (Fig. 7 *B* and *C*); the simulated tip had to approach closer to the surface to show repulsion above both the adsorbed and the lattice oxygen atoms.

The attractive interaction in the simulated $F(z)$ curves has a pure van der Waals character. When the van der Waals correction is switched off in the calculations, there is no attraction in the simulated $F(z)$ curves (*SI Appendix*, Fig. S7). The imaging contrast is therefore based on a combination of electrostatic and Pauli repulsions between tip and surface O atoms. The absence of strong chemical interaction makes these tips easy to use and stable over long periods of time. We also simulated $F(z)$ curves with the same tip cluster but with different orientation with respect to the surface to increase the van der Waals attractive interaction. They are shown in *SI Appendix*, Fig. S8 and display deeper attraction minima.

Discussion

Adsorption and Charge State of O_2. The key requirement to unambiguously observing the molecularly adsorbed oxygen species is

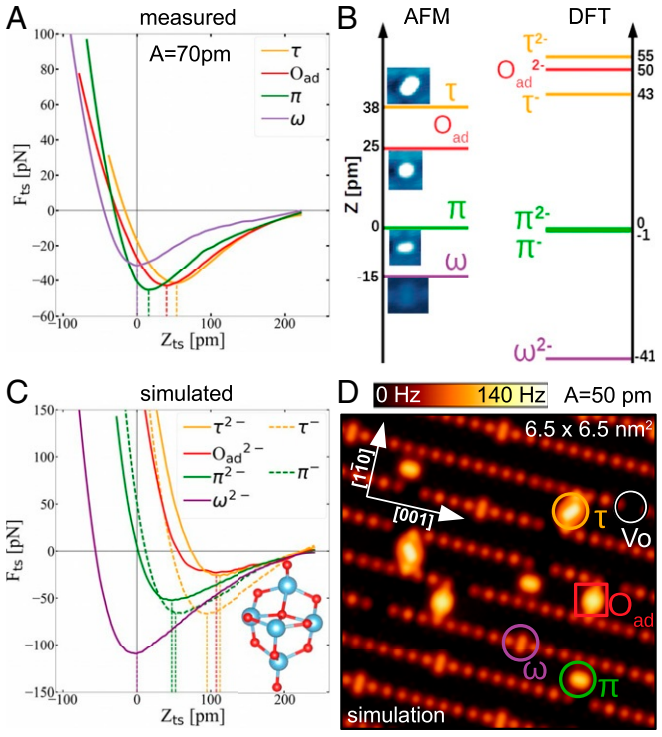

Fig. 7. Height of the adsorbed species. (*A*) Experimental force–distance $F_{ts}(z)$ curves obtained above each of the adsorbates. (*B*) Comparison of the measured height (minimum of $F_{ts}(z)$, *Left*) and calculated height (*Right*) of the adsorbed species. (*C*) Simulated $F_{ts}(z)$ curves obtained with a nonreactive O-terminated $(TiO_2)_5$ tip, illustrated in *Inset*. (*D*) Simulated constant-height AFM image constructed by the simulated tip-sample forces seen in *C*.

measuring with AFM at zero sample bias, i.e., with no charge injection into the molecules. Under these conditions, the ω molecule is imaged as a two-atom feature within an O_{br} row, while the π and τ molecules are observed as two distinct species. This allows us to clearly identify the geometries of O_2/V_O and O_2/Ti_{5c}, whose existence was previously inferred from the disappearance of the oxygen vacancies or the appearance of faint features on the Ti_{5c} rows after O_2 exposure, respectively, by using very gentle conditions in STM (45–49). With the unambiguous insight into the adsorption configurations, we can exclude some theoretically proposed adsorption configurations and confirm the presence of theoretically proposed ω (50–56), π (51–54, 56), and τ (50–59) molecules only. Our work does not provide any indication of other proposed species, such as the tetraoxygen (84, 85).

The charge state of adsorbed O_2 molecules is a longstanding question in oxygen chemistry. Besides quantitative measures of the charge of the stable molecules in calculations (Figs. 1*H* and 2*C*), we additionally assign their charge state through the clear charge transfer from the subsurface electronic polarons to the adsorbed molecules, seen by comparing the electronic structure prior to and after the simulated O_2 adsorption. Within the scope of DFT+U calculations presented here, all superoxo species are metastable with respect to the peroxo species. The imaging setup used in this work provides little direct information on this topic, but comparison of the calculated and measured adsorption geometries strongly supports the peroxo charge state for all adsorbed molecules. There is no significant variation in the apparent height or adsorption geometry between adatoms or molecules of the same type, which makes it unlikely that the same species with different charge states coexist on the surface.

When comparing the thermodynamical stability of the superoxo and peroxo species, none of the superoxo species would be preferred, even if they have to compete for electrons with peroxo species. Our calculations show that, of all combinations, only two superoxo τ molecules would be preferred to one peroxo τ molecule, at extremely high O_2 chemical potentials, above -0.1 eV, which corresponds to temperatures below 150 K at a pressure of 10 bar. However, even this preference is lost because it is energetically downhill to convert two superoxo τ molecules into one peroxo π molecule and one gas molecule.

The calculated adsorption energies of the peroxo species are -1.17 and -1.53 eV for the τ and π molecules, respectively, which is consistent with the desorption peak found in TPD at $\approx$400 K (31–33, 37, 39). The adsorption energies corresponding to the TPD data are between 1.0 and 1.2 eV, close to our calculated values. It is important to consider the chemical potential of an electron when comparing the TPD data with the energies obtained via DFT: Electrons donated by oxygen vacancies lie very close to the conduction band in DFT calculations, while the experimental Fermi level is typically 0.2 to 0.3 eV lower due to the band bending induced by the adsorbed oxygen (86). The experimental adsorption energies may be therefore lower by $2\times$ the value of the band bending ($2\times$ for the peroxo charge state), which provides a reasonable match for both the τ and π molecules in the peroxo configuration.

Assuming that all of the molecular species are in the peroxo charge state, the ω molecules use all excess charge provided by the surface oxygen vacancies, while the other chemisorbed species must drain electrons from subsurface dopants, *i.e.*, interstitial Ti atoms (28, 62, 87) or bulk oxygen vacancies (88). They donate electrons for further chemisorption of π and τ molecules dosed at 80 K, up to a saturation coverage of 0.5 to 1 per oxygen vacancy. It is noteworthy that all of the molecular species are oriented parallel to the surface, making them hard to detect in infrared absorption techniques (89). Also, their peroxo state makes them undetectable by electron paramagnetic resonance (90). Electron energy loss spectroscopy measurements on O_2-exposed rutile TiO_2(110) surfaces support the peroxo charge-state assignment (49).

Thermally Activated Processes. Our results show that the vacancy-mediated dissociation channel (21, 29, 30, 41)—the dissociation of ω molecules—becomes active at temperatures around 80 K. The dissociation channel of τ and π molecules along Ti_{5c} rows (23, 26, 30, 47) is activated above 160 K. Our images of the O_2-covered surface at 80 K generally show lower concentrations of isolated oxygen adatoms compared to previous STM works (21, 23, 28–31, 45–49), mainly due to the prevention of artificial, STM-induced dissociation. The large temperature range of the dissociation events indicates that the process is limited by availability of electrons rather than thermal barriers for dissociation; the dissociation reactions require excess electrons from the substrate:

$$\begin{aligned}\omega^{2-} + 2e^- &\rightarrow O_{ad}^{2-} + O_{br}^{2-}\\ \pi^{2-} + 2e^- &\rightarrow 2\times O_{ad}^{2-}\\ \tau^{2-} + 2e^- &\rightarrow 2\times O_{ad}^{2-}.\end{aligned} \qquad [4]$$

Each of the thermally activated dissociation reactions drains electrons from the bulk and localizes them at the adsorbed oxygen adatoms. This increases the upward band bending (79) near the surface and makes every further reaction more difficult. The band bending may be counteracted first by thermal excitations of electrons closest to the Fermi level and at higher temperatures by slow diffusion of titanium interstitials Ti_{int} (28, 33, 62, 87) or bulk oxygen vacancies (88) toward the surface.

It is surprising that some of the oxygen vacancies become empty after annealing (Fig. 3*C*), which was also apparent in previous STM studies (31). This indicates competition for electrons at elevated temperatures even between the coadsorbed species. One can consider a case where the excess electrons for dissociating π or τ molecules come from an ω molecule coadsorbed at the surface, leading to its desorption. The energy balance calculated from Fig. 1*H* indicates that such a process could be energetically feasible, while a sole desorption of the ω molecule is unlikely.

UV-Induced Reactions. It is well established that the UV-induced O_2 dissociation is an electron-induced process, while holes induce O_2 desorption (11, 13, 14, 36, 38, 40, 41, 43, 48, 49, 91). For our system, this scenario has been verified by tip-induced electron and hole injection as shown Figs. 5 and 6. Events observed upon UV irradiation have a similar base, but there are differences. First, in STM-induced events we can control the potential, but not the number of electrons. Second, the coupled electron and hole dynamics occurring under UV illumination are not reflected in the tip-induced events.

Our UV irradiation experiments show that the ω molecules are predominantly active for dissociation, while the π and τ species prefer desorption. This can be related to the fact that the π and τ species have an in-gap state (Fig. 1), which allows them to accept thermalized holes. Additionally, they are negatively charged species, electrostatically attracting the holes. This is not the case for the ω species: The original oxygen vacancy is 2+ while the ω molecule is 2−. In other words, the charge of the ω molecule is the same as that of the O_{br} atom that it replaces. Together with the absence of an in-gap state, this results in a preference of ω molecules to electron-mediated events.

Let us now discuss whether the UV-induced photodesorption of O_2 is a one-hole or a two-hole process. Previously, this question was addressed by changing the UV intensity, which changes the hole concentration $[h^+]$; a desorption rate linear (square) in $[h^+]$ indicates a one-hole (two-hole) process (37–39). A one-hole process was suggested based on these measurements, which was

taken as an indication of superoxo species present at the surface (37–43). Our insights on the atomic-level mechanisms indicate that this is not necessarily the case.

We attribute the long tail of desorbing molecules after prolonged UV irradiation (37–39) to the slow desorption of ω molecules. This very low desorption rate makes it difficult to measure the dependence of desorbed ω molecules on the incoming light flux (37–39), and it is consistent with the low cross-section of ω molecules for accepting simultaneously two holes:

$$\omega^{2-} + 2h^+ \rightarrow \mathrm{O_2(gas)}.$$

We observed that the fast initial desorption under UV irradiation (37–39) is due to the desorption of π and τ molecules. Moreover, our data in Fig. 4*B* indicate that the switching between the π and τ molecules is at least as frequent as their desorption at small UV exposures. We propose that a metastable transition state is responsible for this configuration switching. After accepting one hole, a π or τ molecule is transformed into a metastable superoxo species on the $\mathrm{Ti_{5c}}$ row ($\mathrm{O_2^-/Ti_{5c}}$):

$$\left(\pi^{2-} \text{ or } \tau^{2-}\right) + h^+ \rightarrow \mathrm{O_2^-/Ti_{5c}}. \quad \textbf{[5]}$$

This metastable state can either desorb in several ways or revert to the peroxo state with the addition of one electron from the surface. Thermal desorption of metastable superoxo species with a calculated adsorption energy of $E_{\mathrm{ads}} \approx -0.7$ eV is unlikely at the temperature of 80 K in our experiments. We also note that disproportionation, i.e., converting two metastable superoxo molecules into one peroxo molecule and an additional gas molecule, is based on a one-hole process, but the reaction rate would still be proportional to $[\mathrm{h^+}]^2$ like a two-hole process, which does not agree with the literature (37–39).

A possible one-step–one-hole desorption process would be that the metastable superoxo desorbs due to the kinetic energy it gains in the transition from the peroxo state:

$$\mathrm{O_2^-/Ti_{5c}} + E_{\mathrm{kin}} \rightarrow \mathrm{O_2(gas)} + \mathrm{e^-}. \quad \textbf{[6]}$$

This process is more likely for τ molecules than for π molecules, because the adsorption geometry of π^{2-} and π^- is very similar, while the adsorption geometry of τ^{2-} and τ^- significantly differs in both in the rotational angle and height (Fig. 7*B*).

We consider a two-step–two-hole desorption channel of the π^{2-} and τ^{2-} molecules more likely. Under UV irradiation, both electrons and holes are generated. This enables both the hole-induced desorption and the electron-induced readsorption of the metastable superoxo state:

$$\begin{aligned} &\mathrm{O_2^-/Ti_{5c}} + h^+ \rightarrow \mathrm{O_2(gas)} \\ &\mathrm{O_2^-/Ti_{5c}} + e^- \rightarrow \pi^{2-} \text{ or } \tau^{2-}. \end{aligned} \quad \textbf{[7]}$$

Our data on switching between τ and π configurations indicate that these two processes happen with similar probabilities, and more detailed examples are shown in *SI Appendix*, Fig. S9. Assuming the concentrations of UV-generated electrons and holes are proportional to each other, the branching ratio of these desorption and readsorption processes will be constant. Therefore, the desorption rate will depend only on the probability of the initial peroxo to metastable superoxo transition and the branching ratio. Although we have a two-hole process, the desorption rate is thus proportional to the hole concentration $[\mathrm{h^+}]$ and not its square. Within this model, the desorption rate of τ and π molecules would be proportional to $[\mathrm{h^+}]^2$ only if the $\mathrm{O_2}$-covered surface were n-doped and in the absence of upward bend bending, i.e., for a constant electron concentration not depending on the UV intensity. This assumption would, however, lead to a modification of the analysis in (37–39) resulting in a desorption rate proportional to $[\mathrm{h^+}]^{\frac{1}{2}}$, which is unlikely. Therefore, our peroxo assignment of the adsorbed $\mathrm{O_2}$ is consistent with the data of refs. 37–39.

AFM Imaging Mechanism. An important aspect of this work is the AFM imaging with an O-terminated tip. Purposely functionalized tips play a major role for noncontact AFM, and our tip termination results in exceptional resolution and offers many opportunities for the future. The key aspects of this tip termination are its inert character toward the surface oxygen atoms, high stability (it works well for measurements performed at 80 K), and rigid character with respect to lateral bending. When applying the traditional CO-terminated tips to $\mathrm{TiO_2}$ surfaces, we had difficulties with their stronger attractive interaction with surface atoms and low stability during measurements performed at 80 K. Also, the lateral bending of the CO (64, 65), which is a key requirement for submolecular imaging of organic molecules (16), is not helpful on ionic surfaces; it distorts the image and creates artificial lines connecting neighboring anions.

We used the tips prepared on the $\mathrm{O_2}$-$\mathrm{TiO_2}$ system for imaging other metal oxides, with a significant success—see images of $\mathrm{In_2O_3}$ (92–94) in *SI Appendix*, Fig. S10 as an example. Oxygen-terminated tips have also been reported to be successful in imaging CuO thin films (95, 96). The main obstacle is the difficulty to functionalize the tip in the desired way. We were unable to obtain this functionalization on clean $\mathrm{TiO_2}$ surfaces; the oxygen could be picked from a chemisorbed $\mathrm{O_2}$ molecule only by dissociating it by a positive sample bias voltage pulse, while the tip is close enough to "catch" one of the O atoms, while the other one remains on the surface. On the other hand, the data reported on CuO thin films indicate easy functionalization. It is likely that the enthalpy of oxide formation (97) plays a role here—it is energetically expensive to extract a single atom from the $\mathrm{TiO_2}$ lattice, while the energy cost on copper oxide is much lower.

Summary and Conclusions

We identified all adsorption configurations of molecular $\mathrm{O_2}$ species observed on the rutile $\mathrm{TiO_2}(110)$ surface. This was made possible through the use of nonintrusive nc-AFM imaging, which reveals the true adsorption geometry without interfering with the surface. Three molecular $\mathrm{O_2}$ species were observed: two adsorbed on the $\mathrm{Ti_{5c}}$ rows and one adsorbed in the oxygen vacancy. Oxygen atoms sitting above $\mathrm{Ti_{5c}}$ atoms are a result of the molecular dissociation through two dissociation channels: vacancy-assisted dissociation with an onset temperature below 80 K and dissociation of molecules on the $\mathrm{Ti_{5c}}$ rows above 160 K. At room temperature, no molecules are left inside oxygen vacancies, but some remain on the $\mathrm{Ti_{5c}}$ rows, giving rise to the TPD peak around 400 K. The adsorption was simulated using DFT+U on a reduced slab and all of the molecular adsorbates were assigned to be peroxo $\mathrm{O_2^{2-}}$, while the adatoms are doubly ionized $\mathrm{O_{ad}^{2-}}$. The calculations show charge transfer from the polaron-hosting $\mathrm{Ti_{6c}}$ sites to the adsorbed oxygen species followed by a change or complete disappearance of the in-gap state characterizing a reduced slab with oxygen vacancies. $\mathrm{O_2/Ti_{5c}}$ molecules prefer photodesorption under UV irradiation, while $\mathrm{O_2/V_O}$ mostly dissociate under the same conditions. We confirm that the dissociation of $\mathrm{O_2}$ is electron mediated, while desorption is a hole-mediated process, by injecting or removing electrons using an STM tip. Within our model, the desorption of $\mathrm{O_2/Ti_{5c}}$ is either a one-step–one-hole process, where the single hole can desorb a peroxo molecule, or a two-step–two-hole process with an intermediate, metastable superoxo state. The clear imaging contrast in AFM images is due to the use of passivated

O-terminated tips. We confirm that the small attractive force between the tip and the adsorbates has a purely van der Waals character. This type of tip termination shows promise for further studies of oxide surfaces.

Methods

The experiments were performed in an ultrahigh-vacuum (UHV) chamber with a base pressure below 2×10^{-11} mbar, equipped with a custom-modified Omicron qPlus LT head, operated at 80 K, except for Fig. 1*A*. Measurements were performed using qPlus sensors with a separate channel for the tunneling current (98). The deflection signal was measured with a cryogenic differential in-vacuum preamplifier (99). Electrochemically etched tungsten tips were glued to the tuning fork and cleaned by field emission and self-sputtering in 2×10^{-6} mbar Ar^+ (100). The tips were treated by controlled touching of the rutile TiO_2(110) surface and subsequently functionalized with an oxygen at the tip apex by applying voltage pulses above the adsorbed O_2 molecules. The rutile TiO_2 sample was cleaned by cycles of 1.5-keV, Ar^+ ion sputtering (10 min, 1 $\mu A \cdot cm^{-2}$), followed by annealing up to 970 K in UHV. The clean surface was inspected with AFM and STM and revealed a (1×1) termination with V_Os with a density ranging from 5 to 12%. Molecular O_2 (99.99%) was dosed at 10 or 80 K by backfilling the chamber with a leak valve, and the measurements were performed at liquid helium (LHe) and liquid nitrogen (LN_2) temperatures, respectively. We note that the crystal is insulating at 4.8 K. UV from a standard Hg source (254 nm) was directed to the sample at LN_2 temperature through a quartz window, after the tip was sufficiently moved to prevent shadowing of the incoming light. A lamp power of 20 W in the UV irradiation experiments corresponds to a photon flux of roughly 1×10^{15} $cm^{-2} \cdot s^{-1}$.

The DFT calculations were performed with the Vienna Ab initio Simulation Package (VASP) (101, 102) and employed the generalized gradient approximation (GGA) within the Perdew, Burke, and Ernzerhof parameterization (103, 104). The van der Waals interactions were included as proposed by Dion et al. (105). The Ti 3*d* orbitals were treated with an on-site effective *U* (106) of 3.9 eV, previously determined by constrained random-phase calculations on bulk rutile titania (66).

The TiO_2(110) surface was modeled by constructing a 6×2 slab with five TiO_2 layers. The bottom two layers were kept fixed, while the top three layers were relaxed with a convergence criterion of 0.01 eV/Å, using an energy cutoff for the plane-wave basis set of 400 eV and a reciprocal-space sampling at the Γ point only. The adsorption energies of molecular $E_{ads}^{O_2}$ and atomic E_{ads}^{O} oxygen species were calculated as

$$E_{ads}^{O_2(O)} = E_{TiO_2+O_2(O)} - (E_{TiO_2} + E_{O_2(O_2/2)}),$$

where E_{TiO_2} is the total energy of the minimum-energy, polaron-hosting ground state of the clean slab reduced by one V_O, $E_{TiO_2+O_2(O)}$ is the total energy of the surface slab with the adsorbed molecular (atomic) oxygen, and $E_{O_2(O_2/2)}$ represents the energy of the O_2 molecule (half the energy of the molecule when calculating the adsorption energy of the adatom) in the gas phase.

Experimental frequency shift vs. distance curves were averaged over at least five curves and transformed to force–distance curves with the Sader inversion equation (107). The long-range background was estimated by measuring $F(z)$ curves above the Ti_{5c} rows and subtracted from the experimental curves. The simulated force curves were obtained by explicitly including an oxygen-terminated $(TiO_2)_5$ tip cluster (80–82) in a 34-Å thick vacuum region above the surface and performing accurate DFT calculations above each adsorbed species, with an approach step size of 25 pm. The bottom five atoms of the tip cluster, together with the top three layers of the surface slab, were relaxed with a more stringent relaxation convergence criterion of 0.005 eV/Å.

Data Availability. All relevant data are included herein or in *SI Appendix*.

ACKNOWLEDGMENTS. We thank Milica Todorović for providing us with the tip model used for simulating force–distance curves. This work was supported by the European Research Council (ERC) Advanced Research Grant "OxideSurfaces" and Austrian Science Fund Projects Wittgenstein Prize (Z 250), Doctoral College "Solids4Fun" (W 1243), "POLOX" (I 2460), and Collaborative Research Center (SFB) "FOXSI" (F45). The computational results were achieved by using the Vienna Scientific Cluster.

1. A. Gurlo, R. Riedel, In situ and operando spectroscopy for assessing mechanisms of gas sensing. *Angew. Chem. Int. Ed.* **46**, 3826–3848 (2007).
2. Z. Guo *et al.*, Recent advances in heterogeneous selective oxidation catalysis for sustainable chemistry. *Chem. Soc. Rev.* **43**, 3480–3524 (2014).
3. J. H. Montoya *et al.*, Materials for solar fuels and chemicals. *Nat. Mater.* **16**, 70–81 (2017).
4. M. Setvín *et al.*, Following the reduction of oxygen on TiO_2 anatase (101) step by step. *J. Am. Chem. Soc.* **138**, 9565–9571 (2016).
5. K. Szot *et al.*, TiO_2–A prototypical memristive material. *Nanotechnology* **22**, 254001 (2011).
6. U. Diebold, The surface science of titanium dioxide. *Surf. Sci. Rep.* **48**, 53–229 (2003).
7. T. L. Thompson, J. T. Yates. Surface science studies of the photoactivation of TiO_2 new photochemical processes. *Chem. Rev.* **106**, 4428–4453 (2006).
8. A. Fujishima, X. Zhang, D. A. Tryk, TiO_2 photocatalysis and related surface phenomena. *Surf. Sci. Rep.* **63**, 515–582 (2008).
9. C. L. Pang, R. Lindsay, G. Thornton, Chemical reactions on rutile TiO_2(110). *Chem. Soc. Rev.* **37**, 2328–2353 (2008).
10. L.-M. Liu, P. Crawford, P. Hu, The interaction between adsorbed OH and O_2 on TiO_2 surfaces. *Prog. Surf. Sci.* **84**, 155–176 (2009).
11. J. T. Yates Jr., Photochemistry on TiO_2: Mechanisms behind the surface chemistry. *Surf. Sci.* **603**, 1605–1612 (2009).
12. Z. Dohnálek, I. Lyubinetsky, R. Rousseau, Thermally-driven processes on rutile TiO_2(110)-(1 × 1): A direct view at the atomic scale. *Prog. Surf. Sci.* **85**, 161–205 (2010).
13. M. A. Henderson, I. Lyubinetsky, Molecular-level insights into photocatalysis from scanning probe microscopy studies on TiO_2(110). *Chem. Rev.* **113**, 4428–4455 (2013).
14. Q. Guo *et al.*, Elementary photocatalytic chemistry on TiO_2 surfaces. *Chem. Soc. Rev.* **45**, 3701–3730 (2016).
15. S. Morita, F. J. Giessibl, E. Meyer, R. Wiesendanger, *Noncontact Atomic Force Microscopy* (Springer, 2015), vol. 3.
16. L. Gross, F. Mohn, N. Moll, P. Liljeroth, G. Meyer, The chemical structure of a molecule resolved by atomic force microscopy. *Science* **325**, 1110–1114 (2009).
17. Y. Sugimoto *et al.*, Chemical identification of individual surface atoms by atomic force microscopy. *Nature* **446**, 64–67 (2007).
18. L. Gross, F. Mohn, P. Liljeroth, F. J. Giessibl, G. Meyer, Measuring the charge state of an adatom with noncontact atomic force microscopy. *Science* **324**, 1428–1431 (2009).
19. B. de la Torre *et al.*, Non-covalent control of spin-state in metal-organic complex by positioning on N-doped graphene. *Nat. Commun.* **9**, 2831 (2018).
20. S. Fatayer *et al.*, Molecular structure elucidation with charge-state control. *Science* **365**, 142–145 (2019).
21. Y. Du, Z. Dohnalek, I. Lyubinetsky, Transient mobility of oxygen adatoms upon O_2 dissociation on reduced TiO_2(110). *J. Phys. Chem. C* **112**, 2649–2653 (2008).
22. N. G. Petrik *et al.*, Chemical reactivity of reduced TiO_2(110): The dominant role of surface defects in oxygen chemisorption. *J. Phys. Chem. C* **113**, 12407–12411 (2009).
23. Y. Du *et al.*, Formation of O adatom pairs and charge transfer upon O_2 dissociation on reduced TiO_2(110). *Phys. Chem. Chem. Phys.* **12**, 6337–6344 (2010).
24. A. C. Papageorgiou *et al.*, Electron traps and their effect on the surface chemistry of TiO_2(110). *Proc. Natl. Acad. Sci. U.S.A.* **107**, 2391–2396 (2010).
25. E. Arima, H. F. Wen, Y. Naitoh, Y. J. Li, Y. Sugawara, KPFM/AFM imaging on TiO_2(110) surface in O_2 gas. *Nanotechnology* **29**, 105504 (2018).
26. Q. Zhang *et al.*, Measurement and manipulation of the charge state of an adsorbed oxygen adatom on the rutile TiO_2(110)-1×1 surface by nc-AFM and KPFM. *J. Am. Chem. Soc.* **140**, 15668–15674 (2018).
27. Y. Adachi *et al.*, Tip-induced control of charge and molecular bonding of oxygen atoms on the rutile TiO_2(110) surface with atomic force microscopy. *ACS Nano* **13**, 6917–6924 (2019).
28. S. Wendt *et al.*, The role of interstitial sites in the Ti3d defect state in the band gap of titania. *Science* **320**, 1755–1759 (2008).
29. S. Wendt *et al.*, Oxygen vacancies on TiO_2(110) and their interaction with H_2O and O_2: A combined high-resolution STM and DFT study. *Surf. Sci.* **598**, 226–245 (2005).
30. E. Lira *et al.*, Dissociative and molecular oxygen chemisorption channels on reduced rutile TiO_2(110): An STM and TPD study. *Surf. Sci.* **604**, 1945–1960 (2010).
31. E. Lira *et al.*, Effects of the crystal reduction state on the interaction of oxygen with rutile TiO_2(110). *Catal. Today* **182**, 25–38 (2012).
32. T. L. Thompson, O. Diwald, J. T. Yates Jr., Molecular oxygen-mediated vacancy diffusion on TiO_2(110)-new studies of the proposed mechanism. *Chem. Phys. Lett.* **393**, 28–30 (2004).
33. E. Lira *et al.*, The importance of bulk Ti^{3+} defects in the oxygen chemistry on titania surfaces. *J. Am. Chem. Soc.* **133**, 6529–6532 (2011).
34. M. A. Henderson, W. S. Epling, C. L. Perkins, C. H. F. Peden, U. Diebold, Interaction of molecular oxygen with the vacuum-annealed TiO_2(110) surface: Molecular and dissociative channels. *J. Phys. Chem. B* **103**, 5328–5337 (1999).
35. T. Berger, M. Sterrer, O. Diwald, E. Knözinger, Charge trapping and photoadsorption of O_2 on dehydroxylated TiO_2 nanocrystals-an electron paramagnetic resonance study. *ChemPhysChem* **6**, 2104–2112 (2005).
36. J. Lee, Z. Zhang, J. T. Yates Jr., Electron-stimulated positive-ion desorption caused by charge transfer from adsorbate to substrate: Oxygen adsorbed on TiO_2(110). *Phys. Rev. B* **79**, 081408 (2009).
37. T. L. Thompson, J. T. Yates, Monitoring hole trapping in photoexcited TiO_2(110) using a surface photoreaction. *J. Phys. Chem. B* **109**, 18230–18236 (2005).
38. T. L. Thompson, J. T. Yates, Control of a surface photochemical process by fractal electron transport across the surface: O_2 photodesorption from TiO_2(110). *J. Phys. Chem. B* **110**, 7431–7435 (2006).
39. D. Sporleder, D. P. Wilson, M. G. White, Final state distributions of O_2 photodesorbed from TiO_2(110). *J. Phys. Chem. C* **113**, 13180–13191 (2009).
40. Z. Zhang, J. T. Yates Jr., Direct observation of surface-mediated electron-hole pair recombination in TiO_2(110). *J. Phys. Chem. C* **114**, 3098–3101 (2010).

41. N. G. Petrik, G. A. Kimmel, Photoinduced dissociation of O_2 on rutile TiO_2(110). *J. Phys. Chem. Lett.* **1**, 1758–1762 (2010).
42. N. G. Petrik, G. A. Kimmel, Electron- and hole-mediated reactions in UV-irradiated O_2 adsorbed on reduced rutile TiO_2(110). *J. Phys. Chem. C* **115**, 152–164 (2011).
43. N. G. Petrik, G. A. Kimmel, Oxygen photochemistry on TiO_2(110): Recyclable, photoactive oxygen produced by annealing adsorbed O_2. *J. Phys. Chem. Lett.* **2**, 2790–2796 (2011).
44. N. G. Petrik, G. A. Kimmel, Probing the photochemistry of chemisorbed oxygen on TiO_2(110) with Kr and other co-adsorbates. *Phys. Chem. Chem. Phys.* **16**, 2338–2346 (2014).
45. P. Scheiber, A. Riss, M. Schmid, P. Varga, U. Diebold, Observation and destruction of an elusive adsorbate with STM: O_2/TiO_2(110). *Phys. Rev. Lett.* **105**, 216101 (2010).
46. S. Tan *et al.*, Molecular oxygen adsorption behaviors on the rutile TiO_2(110)-1$\times$1 surface: An in situ study with low-temperature scanning tunneling microscopy. *J. Am. Chem. Soc.* **133**, 2002–2009 (2011).
47. Z.-T. Wang, Y. Du, Z. Dohnálek, I. Lyubinetsky, Direct observation of site-specific molecular chemisorption of O_2 on TiO_2(110). *J. Phys. Chem. Lett.* **1**, 3524–3529 (2010).
48. Z.-T. Wang, N. Aaron Deskins, I. Lyubinetsky, Direct imaging of site-specific photocatalytical reactions of O_2 on TiO_2(110). *J. Phys. Chem. Lett.* **3**, 102–106 (2011).
49. M. A. Henderson, M. Shen, Z.-T. Wang, I. Lyubinetsky, Characterization of the active surface species responsible for UV-induced desorption of O_2 from the rutile TiO_2(110) surface. *J. Phys. Chem. C* **117**, 5774–5784 (2013).
50. X. Wu, A. Selloni, M. Lazzeri, S. K. Nayak, Oxygen vacancy mediated adsorption and reactions of molecular oxygen on the TiO_2(110) surface. *Phys. Rev. B* **68**, 241402 (2003).
51. M. D. Rasmussen, L. M. Molina, B. Hammer, Adsorption, diffusion, and dissociation of molecular oxygen at defected TiO_2(110): A density functional theory study. *J. Chem. Phys.* **120**, 988–997 (2004).
52. S. Chrétien, H. Metiu, O_2 evolution on a clean partially reduced rutile TiO_2(110) surface and on the same surface precovered with Au_1 and Au_2: The importance of spin conservation. *J. Chem. Phys.* **129**, 074705 (2008).
53. Y. Ji, B. Wang, Y. Luo, First principles study of O_2 adsorption on reduced rutile TiO_2(110) surface under UV illumination and its role on CO oxidation. *J. Phys. Chem. C* **117**, 956–961 (2013).
54. H. Xu, S. Y. Tong, Interaction of O_2 with reduced rutile TiO_2(110) surface. *Surf. Sci.* **610**, 33–41 (2013).
55. H. Tian, B. Xu, J. Fan, H. Xu, Intrinsic role of excess electrons in surface reactions on rutile TiO_2(110): Using water and oxygen as probes. *J. Phys. Chem. C* **122**, 8270–8276 (2018).
56. A. Tilocca, A. Selloni, O_2 and vacancy diffusion on rutile (110): Pathways and electronic properties. *ChemPhysChem* **6**, 1911–1916 (2005).
57. L. M. Molina, M. D. Rasmussen, B. Hammer, Adsorption of O_2 and oxidation of CO at Au nanoparticles supported by TiO_2(110). *J. Chem. Phys.* **120**, 7673–7680 (2004).
58. S. Chrétien, H. Metiu, Enhanced adsorption energy of Au_1 and O_2 on the stoichiometric TiO_2(110) surface by coadsorption with other molecules. *J. Chem. Phys.* **128**, 044714 (2008).
59. N. Aaron Deskins, R. Rousseau, M. Dupuis, Defining the role of excess electrons in the surface chemistry of TiO_2. *J. Phys. Chem. C* **114**, 5891–5897 (2010).
60. V. E. Henrich, P. Anthony Cox, *The Surface Science of Metal Oxides* (Cambridge University Press, 1996).
61. Z. Dohnálek, J. Kim, O. Bondarchuk, J. M. White, B. D. Kay, Physisorption of N_2, O_2, and CO on fully oxidized TiO_2(110). *J. Phys. Chem. B* **110**, 6229–6235 (2006).
62. Z. Zhang *et al.*, Unraveling the diffusion of bulk Ti interstitials in rutile TiO_2(110) by monitoring their reaction with O adatoms. *J. Phys. Chem. C* **114**, 3059–3062 (2010).
63. U. Diebold, J. F. Anderson, K.-O. Ng, D. Vanderbilt, Evidence for the tunneling site on transition-metal oxides: TiO_2(110). *Phys. Rev. Lett.* **77**, 1322–1325 (1996).
64. P. Hapala *et al.*, Mechanism of high-resolution STM/AFM imaging with functionalized tips. *Phys. Rev. B* **90**, 085421 (2014).
65. M. Ellner *et al.*, The electric field of CO tips and its relevance for atomic force microscopy. *Nano Lett.* **16**, 1974–1980 (2016).
66. M. Setvín *et al.*, Direct view at excess electrons in TiO_2 rutile and anatase. *Phys. Rev. Lett.* **113**, 086402 (2014).
67. M. Reticcioli *et al.*, Polaron-driven surface reconstructions. *Phys. Rev. X* **7**, 031053 (2017).
68. M. Reticcioli, M. Setvín, M. Schmid, U. Diebold, C. Franchini, Formation and dynamics of small polarons on the rutile TiO_2(110) surface. *Phys. Rev. B* **98**, 045306 (2018).
69. M. Reticcioli, U. Diebold, G. Kresse, C. Franchini, "Small polarons in transition metal oxides" in *Handbook of Materials Modeling*, W. Andreoni, S. Yip, Eds. (Springer, Cham, Switzerland, 2019), pp. 1035–1073.
70. M. Reticcioli *et al.*, Interplay between adsorbates and polarons: CO on rutile TiO_2(110). *Phys. Rev. Lett.* **122**, 016805 (2019).
71. R. F. W. Bader, Atoms in molecules. *Acc. Chem. Res.* **18**, 9–15 (1985).
72. T. Akbay *et al.*, The interaction of molecular oxygen on LaO terminated surfaces of $LaNiO_4$. *J. Mater. Chem.* **4**, 13113–13124 (2016).
73. G. Preda, G. Pacchioni, Formation of oxygen active species in Ag-modified CeO_2 catalyst for soot oxidation: A DFT study. *Catal. Today* **177**, 31–38 (2011).
74. Z. Chen, J. Li, X. C. Zeng, Unraveling oxygen evolution in Li-rich oxides: A unified modeling of the intermediate peroxo/superoxo-like dimers. *J. Am. Chem. Soc.* **141**, 10751–10759 (2019).
75. C. J. Kramer, W. B. Tolman, K. H. Theopold, A. L. Rheingold, Variable character of O-O and M-O bonding in side-on (η^2) 1:1 metal complexes of O_2. *Proc. Natl. Acad. Sci. U.S.A.* **100**, 3635–3640 (2003).
76. O. Krejčí, P. Hapala, M. Ondráček, P. Jelínek, Principles and simulations of high-resolution STM imaging with a flexible tip apex. *Phys. Rev. B* **95**, 045407 (2017).
77. B. de la Torre *et al.*, Submolecular resolution by variation of the inelastic electron tunneling spectroscopy amplitude and its relation to the AFM/STM signal. *Phys. Rev. Lett.* **119**, 166001 (2017).
78. C. Barth, A. S. Foster, C. R. Henry, A. L. Shluger, Recent trends in surface characterization and chemistry with high-resolution scanning force methods. *Adv. Mater.* **23**, 477–501 (2011).
79. M. Setvín, J. Hulva, G. S. Parkinson, M. Schmid, U. Diebold, Electron transfer between anatase TiO_2 and an O_2 molecule directly observed by atomic force microscopy. *Proc. Natl. Acad. Sci. U.S.A.* **114**, E2556–E2562 (2017).
80. M. J. Lundqvist, M. Nilsing, P. Persson, S. Lunell, DFT study of bare and dye-sensitized TiO_2 clusters and nanocrystals. *Int. J. Quant. Chem.* **106**, 3214–3234 (2006).
81. A. Yurtsever *et al.*, Understanding image contrast formation in $TiO_2$with force spectroscopy. *Phys. Rev. B* **85**, 125416 (2012).
82. O. Stetsovych *et al.*, Atomic species identification at the (101) anatase surface by simultaneous scanning tunnelling and atomic force microscopy. *Nat. Commun.* **6**, 7265 (2015).
83. F. J. Giessibl, Forces and frequency shifts in atomic-resolution dynamic-force microscopy. *Phys. Rev. B* **56**, 16010–16015 (1997).
84. D. Pillay, Y. Wang, G. S. Hwang, Prediction of tetraoxygen formation on rutile TiO_2(110). *J. Am. Chem. Soc.* **128**, 14000–14001 (2006).
85. G. A. Kimmel, N. G. Petrik, Tetraoxygen on reduced TiO_2(110): Oxygen adsorption and reactions with bridging oxygen vacancies. *Phys. Rev. Lett.* **100**, 196102 (2008).
86. Z. Zhang, J. T. Yates Jr., Band bending in semiconductors: Chemical and physical consequences at surfaces and interfaces. *Chem. Rev.* **112**, 5520–5551 (2012).
87. M. Bowker, R. A. Bennett, The role of Ti^{3+} interstitials in TiO_2(110) reduction and oxidation. *J. Phys. Condens. Matter* **21**, 474224 (2009).
88. M. Li *et al.*, The influence of the bulk reduction state on the surface structure and morphology of rutile TiO_2(110) single crystals. *J. Phys. Chem. B* **104**, 4944–4950 (2000).
89. C. Yang, C. Wöll, IR spectroscopy applied to metal oxide surfaces: Adsorbate vibrations and beyond. *Adv. Phys. X* **2**, 373–408 (2017).
90. A. Abragam, B. Bleaney, *Electron Paramagnetic Resonance of Transition Ions* (Oxford University Press, Oxford, UK, 2012).
91. M. A. Henderson, A surface science perspective on TiO_2 photocatalysis. *Surf. Sci. Rep.* **66**, 185–297 (2011).
92. M. Wagner *et al.*, Reducing the In_2O_3(111) surface results in ordered indium adatoms. *Adv. Mater. Interfaces* **1**, 1400289 (2014).
93. M. Wagner *et al.*, Resolving the structure of a well-ordered hydroxyl overlayer on In_2O_3(111): Nanomanipulation and theory. *ACS Nano* **11**, 11531–11541 (2017).
94. M. Wagner *et al.*, Prototypical organic-oxide interface: Intramolecular resolution of sexiphenyl on In_2O_3(111). *ACS Appl. Mater. Interfaces* **10**, 14175–14182 (2018).
95. H. Mönig *et al.*, Quantitative assessment of intermolecular interactions by atomic force microscopy imaging using copper oxide tips. *Nat. Nanotechnol.* **13**, 371–375 (2018).
96. L. Alexander, F. J. Giessibl, In-situ characterization of O-terminated Cu tips for high-resolution atomic force microscopy. *Appl. Phys. Lett.* **114**, 143103 (2019).
97. C. T. Campbell, Ultrathin metal films and particles on oxide surfaces: Structural, electronic and chemisorptive properties. *Surf. Sci. Rep.* **27**, 1–111 (1997).
98. F. J. Giessibl, The qPlus sensor, a powerful core for the atomic force microscope. *Rev. Sci. Instrum.* **90**, 011101 (2019).
99. F. Huber, F. J. Giessibl, Low noise current preamplifier for qPlus sensor deflection signal detection in atomic force microscopy at room and low temperatures. *Rev. Sci. Instrum.* **88**, 073702 (2017).
100. M. Setvín *et al.*, Ultrasharp tungsten tips—characterization and nondestructive cleaning. *Ultramicroscopy* **113**, 152–157 (2012).
101. G. Kresse, J. Furthmüller, From ultrasoft pseudopotentials to the projector augmented-wave method. *Phys. Rev. B* **54**, 11169 (1996).
102. G. Kresse, J Furthmüller, Efficiency of ab-initio total energy calculations for metals and semiconductors using a plane-wave basis set. *Comput. Mater. Sci.* **6**, 15–50 (1996).
103. J. P. Perdew, K. Burke, M. Ernzerhof, Generalized gradient approximation made simple. *Phys. Rev. Lett.* **77**, 3865–3868 (1996).
104. J. Klimeš, D. R. Bowler, A. Michaelides, Chemical accuracy for the van der Waals density functional. *J. Phys. Condens. Matter* **22**, 022201 (2009).
105. M. Dion, H. Rydberg, E. Schröder, D. C. Langreth, B. I. Lundqvist, Van der Waals density functional for general geometries. *Phys. Rev. Lett.* **92**, 246401 (2004).
106. S. L. Dudarev, G. A. Botton, S. Y. Savrasov, C. J. Humphreys, A. P. Sutton, Electron-energy-loss spectra and the structural stability of nickel oxide: An LSDA+U study. *Phys. Rev. B* **57**, 1505–1509 (1998).
107. J. E. Sader, S. P. Jarvis, Accurate formulas for interaction force and energy in frequency modulation force spectroscopy. *Appl. Phys. Lett.* **84**, 1801–1803 (2004).